arXiv:2505.01026v1 [physics.optics] 2 May 2025

Bridging Statistical Scattering and Aberration Theory: Ray Deflection Function - II: Numerical Validation

Netzer Moriya

Abstract

This paper presents a comprehensive experimental validation of a recently developed Ray Deflection Function (RDF) approach, which offers a new framework for modeling surface roughness effects in optical systems. Through detailed geometrical ray tracing simulations, we demonstrate that the RDF methodology successfully bridges two traditionally separate domains: statistical scattering models and deterministic aberration analysis. We implement and compare the two approaches for modeling a parabolic mirror with surface imperfections with three cases: (1) an ideal parabolic mirror baseline, (2) the conventional Harvey-Shack (HS) statistical scattering theory applied to ray perturbations, and (3) the newly proposed aberration term method based on the RDF theory. Our results confirm the statistical equivalence between the HS approach and the RDF-based aberration term method, with both producing close near-focal-plane distributions and focal volume characteristics. By establishing this equivalence, we validate that surface roughness effects can be accurately represented as deterministic aberration terms while maintaining fidelity to established statistical scattering models.

1 Introduction

Surface roughness significantly impacts the performance of optical systems, causing scattered light that degrades image quality and reduces contrast. Traditional approaches to modeling the effects of surface roughness typically follow one of two distinct methodologies [1–4]: detailed physical modeling of surface topography with direct ray-tracing, or statistical scatter models that operate primarily in the angular domain. Both approaches present significant limitations—the former is computationally intensive and requires detailed surface data with sophisticated beam-roughness interaction models. The latter, exemplified by Harvey-Shack theory, establishes a direct proportional relationship between the bidirectional reflectance distribution function (BRDF) of a rough surface and

the power spectral density (PSD) of its height variations. While this provides a statistical framework for predicting angular light scattering, it remains fundamentally separate from conventional optical design workflows that use aberration formulations to handle smooth surface deviations but have no established mechanism for incorporating roughness effects.

In our theoretical paper [5], we introduced a new conceptual framework that recasts surface roughness effects as a "ray deflection function" (RDF), which can be statistically represented through a modified Zernike-Fourier hybrid approach. This transformation allows surface roughness to be seamlessly integrated with other optical aberration terms by expressing its effects through equivalent modifications to the ideal mirror shape.

A theoretical analysis justifying the use of ray-based modeling for realistic optical systems with surface roughness is provided in A.

The present paper focuses on the numerical validation of this theoretical framework through detailed simulations. We implement the RDF approach using statistical perturbations to rays reflected from an ideal parabolic mirror and compare the results with conventional Harvey-Shack scatter theory. By demonstrating the statistical equivalence between these approaches, we establish that our method maintains the physical accuracy of established scattering models while offering significant computational advantages and enhanced integration with traditional optical design frameworks.

2 Theoretical Foundation

Prior to presenting our experimental implementation and results, we summarize the key aspects of the RDF theoretical framework to provide context for the validation study (see in [5] and references therein).

2.1 The Ray Deflection Function Concept

We define the Ray Deflection Function (RDF), denoted by $\mathbf{D}(\mathbf{r}_0)$, as the local angular deflection experienced by a ray upon reflection due to a height perturbation at the surface point. For small perturbations under the scalar wave approximation, this deflection can be expressed in terms of the local phase gradient [5]:

$$\mathbf{D}(\mathbf{r}_0) = -\frac{\lambda}{4\pi}\nabla\Phi(x, y) \tag{1}$$

where $\Phi(x, y)$ is the phase delay induced by surface height variations, and λ is the wavelength of light. This relationship is derived from the eikonal approximation and

is valid when surface perturbations are smooth and differentiable, incident and reflected angles are small, and the wavefront phase is well-described by scalar field theory.

The applicability of this geometric ray approach versus diffraction-based modeling for different optical system parameters is analyzed quantitatively in A, where we demonstrate that for practical telescope mirror specifications, geometric effects dominate diffraction effects by several orders of magnitude.

2.2 Relationship to Harvey-Shack Theory

The Harvey-Shack theory [6] establishes that the bidirectional reflectance distribution function (BRDF) is directly proportional to the power spectral density (PSD) of surface height variations:

$$\mathrm{BRDF}(\alpha_s - \alpha_i, \beta_s - \beta_i) \propto \mathrm{PSD}\left(\frac{\alpha_s - \alpha_i}{\lambda}, \frac{\beta_s - \beta_i}{\lambda}\right) \tag{2}$$

where α and β are direction cosines, and subscripts i and s refer to incident and scattered directions, respectively.

Our approach leverages this relationship to derive a ray deflection function that produces the same statistical distribution of scattered rays as would be produced by the physical surface roughness. The key insight is that for many practical applications, the exact physical roughness pattern is less important than its statistical effect on the reflected light distribution.

2.3 Aberration Term Formulation

A central contribution of our theoretical framework is the transformation of statistical surface roughness into equivalent deterministic aberration terms that directly modify the ideal mirror shape. The magnitude of this effective shape change scales with the RMS roughness while preserving the statistical characteristics of the original PSD model.

For a surface with a given PSD, the phase function $\Phi(x, y)$ can be represented using a modified Zernike-Fourier hybrid approach:

$$\Phi(x, y) = \sum_{j=1}^{N} C_j Z_j(x, y) \tag{3}$$

where $Z_j(x, y)$ are Zernike polynomials and the coefficients C_j are statistically determined by the spectral overlap between the PSD and the Fourier transform of each Zernike term:

$$C_j = \sqrt{\omega_j} \cdot \xi_j \tag{4}$$

with ξ_j representing uncorrelated random variables drawn from a standard normal distribution, and ω_j being the spectral weight of each Zernike mode calculated through:

$$\omega_j = \iint \mathrm{PSD}(f_x, f_y)|F_j(f_r, \phi_f)|^2 df_x df_y \tag{5}$$

where $F_j(f_r, \phi_f)$ is the Fourier transform of the j-th Zernike polynomial.

This approach ensures that the statistical properties of the original surface PSD are preserved in the phase function representation. For computational implementation, the series is truncated at N terms based on a variance capture criterion, where the cumulative spectral weight reaches a prescribed fraction of the total surface variance:

$$\frac{\sum_{j=1}^{N} \omega_j}{\sigma^2} \geq 1 - \epsilon \tag{6}$$

with ϵ being a small tolerance parameter (typically 0.01-0.05). The number of required terms depends on the spatial frequency characteristics of the surface roughness, with $N \approx 2\pi R/l_c$ providing a practical guideline for many common PSDs, where R is the aperture radius and l_c is the characteristic correlation length.

This formulation allows roughness effects to be treated as deterministic aberration terms that can be directly integrated with conventional optical design methods, while maintaining statistical fidelity to the underlying roughness model and preserving the spatial correlation structure implied by the original PSD.

3 Ray-Tracing Simulation Principles

The ray-tracing simulation employed in this study systematically evaluates the optical performance of modified mirror surfaces by numerically tracing light rays through defined optical paths. The underlying framework is structured around the precise geometrical representation of mirror surfaces, computation of surface normals, and subsequent calculation of reflected rays. The mathematical principles governing this simulation are outlined below.

3.1 Surface Definition

The mirror surface S is defined as a rotationally symmetric function incorporating a classical parabolic term augmented by higher-order spherical aberrations up to the 12th order[1]. Explicitly, the surface height function $z(\rho)$ in cylindrical coordinates (ρ, θ, z) is represented as:

$$z(\rho) = \frac{\rho^2}{4f} + \sum_{n=2}^{6} c_{2n,0}\rho^{2n} + \xi(\rho, \theta) \tag{7}$$

where f is the focal length of the parabolic reference surface, $\rho = \sqrt{x^2 + y^2}$ denotes the radial coordinate from the optical axis, $c_{2n,0}$ are spherical aberration coefficients characterizing deviations from the ideal parabolic form, and $\xi(\rho, \theta)$ represents the synthetic surface roughness modeled through a hybrid Zernike-Fourier approach, characterized statistically by an RMS height σ.

3.2 Surface Normal Calculation

The unit normal vector $\hat{\mathbf{N}}$ at any surface point $\mathbf{P}(x, y, z)$ is critical for accurately determining reflected rays. It is computed from the gradient of the surface $z(x, y)$:

$$\hat{\mathbf{N}}(x, y) = \frac{(-\frac{\partial z}{\partial x}, -\frac{\partial z}{\partial y}, 1)}{\sqrt{1 + \left(\frac{\partial z}{\partial x}\right)^2 + \left(\frac{\partial z}{\partial y}\right)^2}} \tag{8}$$

Numerical differentiation via central finite differences is employed to approximate the partial derivatives, ensuring computational efficiency and sufficient accuracy:

$$\frac{\partial z}{\partial x} \approx \frac{z(x + h, y) - z(x - h, y)}{2h}, \quad \frac{\partial z}{\partial y} \approx \frac{z(x, y + h) - z(x, y - h)}{2h} \tag{9}$$

where h is a small step size optimized for numerical stability and precision.

3.3 Incident and Reflected Rays

The simulation assumes incident rays are parallel to the optical axis, described by the incident ray vector $\hat{\mathbf{I}} = (0, 0, -1)$. Given the surface normal $\hat{\mathbf{N}}$, the reflected ray direction $\hat{\mathbf{R}}$ is computed according to the classical law of reflection:

[1] In what follows we simulate a parabolic mirror's surface so $c_{2n,0} = 0 \forall n$.

$$\hat{\mathbf{R}} = \hat{\mathbf{I}} - 2(\hat{\mathbf{I}} \cdot \hat{\mathbf{N}})\hat{\mathbf{N}} \tag{10}$$

This formulation ensures the physically accurate reflection of each incident ray on the surface.

3.4 Random Point Sampling

Hit points for ray tracing are randomly selected within the mirror's clear aperture using a uniform distribution subject to a margin exclusion criterion. The selection process ensures points lie within the defined aperture boundary:

$$(x_i, y_i) \in S \quad \text{such that} \quad d((x_i, y_i), \partial S) > d_{\min} \tag{11}$$

where $d_{\min}$ is a user-defined minimum margin to avoid edge anomalies, and ∂S represents the boundary of the mirror aperture. This approach ensures proper sampling across the mirror surface while avoiding potential numerical issues near the edges. The implementation uses a distance-based criterion to identify and exclude points that are too close to the aperture boundary, providing robust sampling for both circular and more complex aperture geometries.

3.5 Geometric Characterization

To validate the accuracy of the mirror geometry prior to ray tracing, geometric properties including vertex location and aperture centroid are calculated via robust iterative methods.

Edge points are accurately localized using binary search algorithms, and Singular Value Decomposition (SVD) is employed for determining the best-fit plane through the aperture circumference points:

$$\mathbf{X}_{\text{circ}} = \{\mathbf{x}_1, \mathbf{x}_2, \ldots, \mathbf{x}_N\}, \quad \mathbf{x}_i \in \partial S \tag{12}$$

The best-fit plane normal $\mathbf{N}_{\text{plane}}$ is found by minimizing residuals δz_i:

$$\min \sum_{i=1}^{N} (\delta z_i)^2, \quad \text{where} \quad \delta z_i = \mathbf{N}_{\text{plane}} \cdot \mathbf{x}_i \tag{13}$$

The standard deviation of residuals provides a quantitative measure of aperture planarity and serves as a quality check before proceeding with the simulation. This ensures

that any observed scattering effects in the results can be attributed to the intentionally introduced surface roughness rather than geometric modeling errors.

3.6 Data Generation and Analysis

The results are compiled into structured data matrices capturing incident and reflected ray vectors, hit points, and surface normals, enabling comprehensive statistical and comparative analysis of optical performance under varied surface modifications and conditions.

This rigorous mathematical and computational framework facilitates an accurate and detailed understanding of optical performance implications arising from surface modifications in advanced optical systems.

3.7 General Simulation Setup

To validate our theoretical framework, we implemented the Ray Deflection Function (RDF) approach using statistical perturbations to rays reflected from an ideal parabolic mirror with optical axis coincident with the z-axis. Our experimental setup consists of a parabolic mirror with focal length $f = 2.8$ m and aperture diameter $A_p = 0.4$ m.

For the simulation of surface roughness, we set the imperfections RMS to be characterized by height $\sigma = 1 \times 10^{-7}$ m (100 nm). This parameter was chosen to represent realistic optical surfaces while remaining well within the validity range of our small-angle approximation. Surface roughness of this magnitude is typical for moderate-quality optical components and falls within practical manufacturing tolerances observed in many optical systems[2].

All simulations were performed using a custom ray-tracing implementation that allows for different surface representation methods and ray perturbation strategies. Statistical analyses were conducted on ensembles of 15,000 rays uniformly distributed across the mirror aperture. The ray interactions and subsequent propagation were analyzed at multiple planes along the optical axis to characterize the reflected rays distribution in the vicinity of the expected focal plane.

[2]Surface roughness parameters such as $\sigma = 100$ nm and $l_c = 1$ mm may represent realistic values for conventionally polished optical surfaces. This combination of RMS height and correlation length is typical for moderate-quality optical components and falls within practical manufacturing tolerances observed in many optical systems.

4 Pure Parabolic Mirror - Baseline Analysis

As a baseline for evaluating the effects of imperfections introduced on the surface of a smooth mirror, we first simulated an ideal parabolic mirror without any surface roughness.

4.1 Mirror Geometry and Ray Reflection

The surface of the ideal parabolic mirror follows the equation:

$$z(x, y) = \frac{x^2 + y^2}{4f} \tag{14}$$

where $f = 2.8$ m is the focal length. Figure 1 shows the three-dimensional visualization of the mirror surface and the two-dimensional profile along the x-axis. The smooth, continuous surface of the ideal parabolic mirror provides a perfect focus at $z = f$.

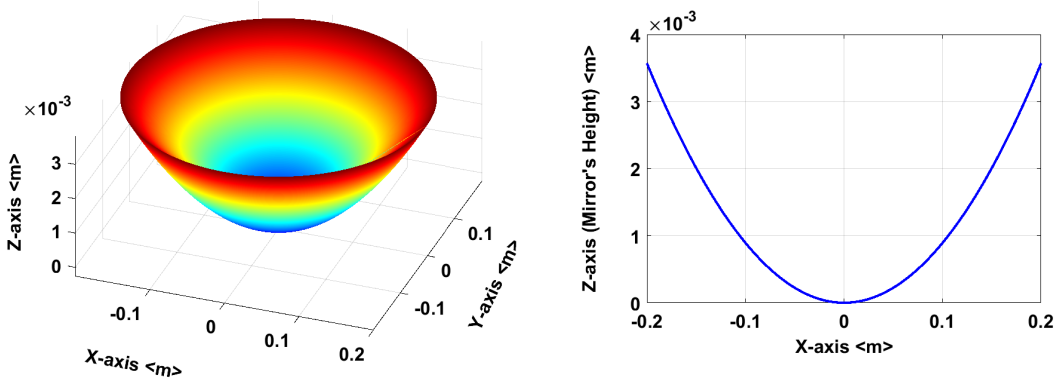

Figure 1: 3D visualization of the ideal parabolic mirror surface with focal length $f = 2.8$ m and aperture diameter $A_p = 0.4$ m. The color gradient represents the surface height (left), and 2D profile of the ideal parabolic mirror along the x-axis. The profile follows the equation $z(x) = x^2/(4f)$ (right).

The points on the mirror's surface where the rays hit and reflected are where selected uniformly in random manner and are show in figure 2

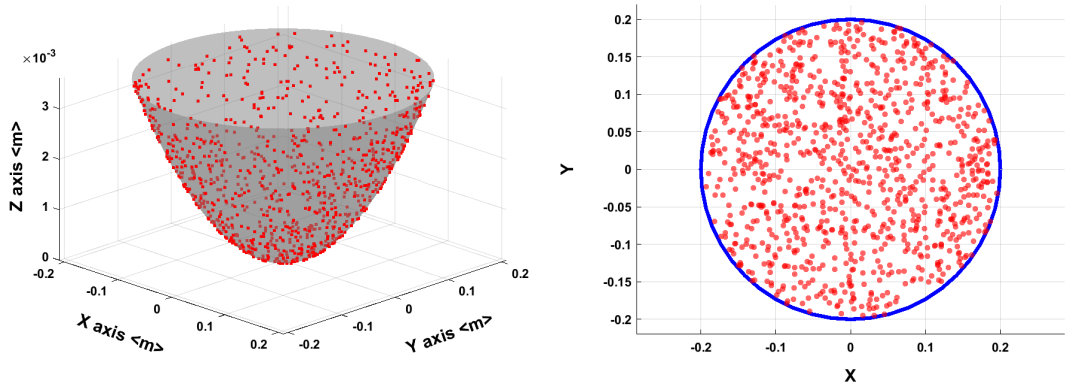

Figure 2: Three-dimensional distribution of randomly selected ray hit points on the mirror surface. The red dots show the uniform distribution of incident ray locations across the mirror's surface (left) and 2D projection of the random ray hit-points on the mirror aperture (right). The uniform distribution ensures comprehensive coverage of the mirror surface for statistical analysis.

The reflection of incident rays parallel to the optical axis was calculated using the standard law of reflection. Figure 3 illustrates the reflected ray pattern, with all rays converging precisely at the focal point. As expected for an ideal parabolic mirror, the ray convergence is perfect, with no aberrations or scattering effects.

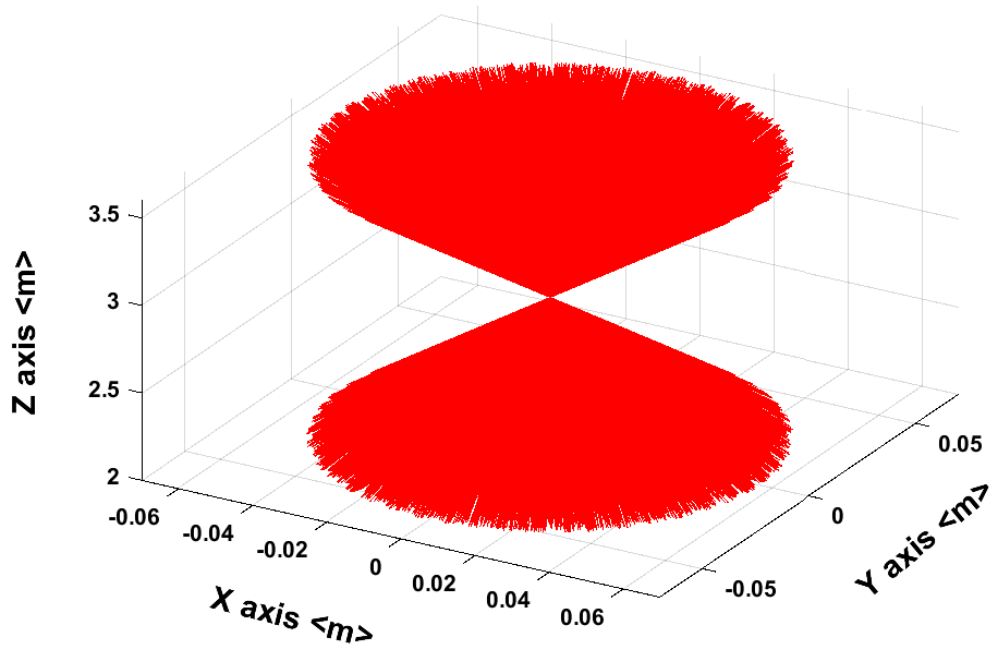

Figure 3: Three-dimensional visualization of the reflected rays from the ideal parabolic mirror. All rays converge at the focal point $z = 2.8$ m, demonstrating perfect focusing behavior with no aberrations.

4.2 Focal Volume Analysis

To quantify the focusing properties of the ideal mirror, we analyzed the distribution of rays passing through planes perpendicular to the optical axis at various positions near the focal region. Figure 4 shows the "ring-through" profile, which represents the number of rays contained within a minimal radius that encloses at least 90% of the total rays at each z position.

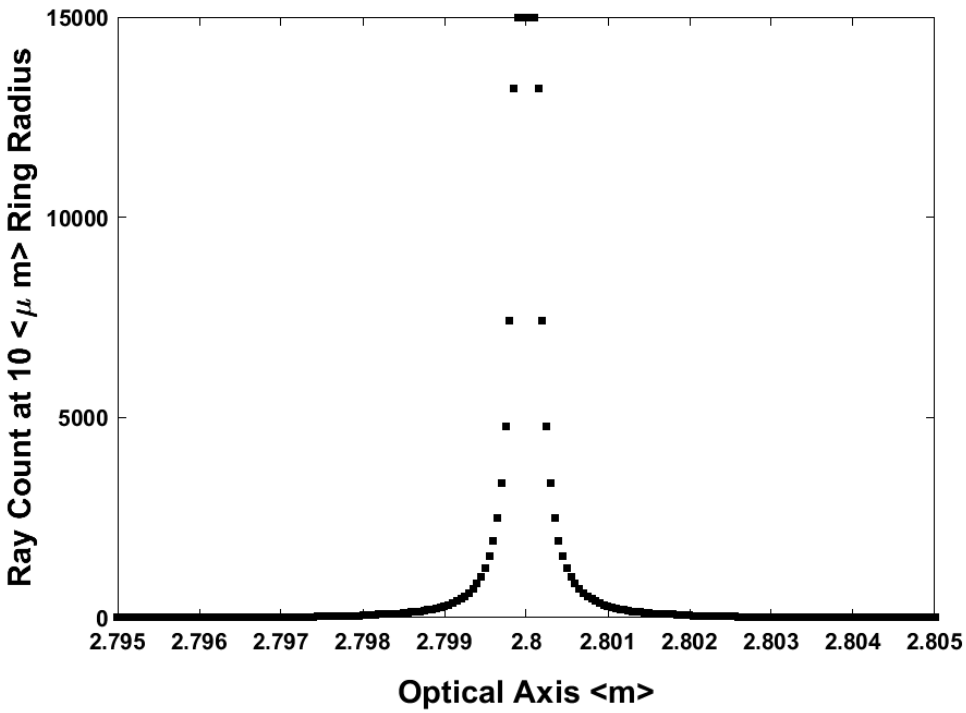

Figure 4: Ray density profile along the optical axis for the ideal parabolic mirror. The plot shows the number of rays contained within a 0.01 mm radius ring at different positions along the z-axis. The sharp peak at $z = 2.8$ m indicates perfect focusing with a FWHM of approximately 0.3 mm.

For the ideal parabolic mirror, this profile shows a sharp peak centered precisely at $z = 2.8$ m, with a narrow full width at half maximum (FWHM) of approximately 0.3 mm. This represents the geometrically perfect focusing performance of an ideal parabolic reflector in the absence of wave effects, and serves as the baseline against which the roughened mirror simulations will be compared.

The ray distribution on planar CCD-like grids perpendicular to the optical axis at three positions near the focus is shown in Figure 15. These images demonstrate the tight concentration of rays at the focal point for the ideal mirror, with minimal spreading as the observation plane moves slightly away from the exact focal position.

5 Harvey-Shack Approach Implementation

Here, the general setup (see Section 3.7) was applied to implement the Harvey-Shack theory for modeling surface roughness effects.

5.1 Implementation Architecture

The implementation constructs a statistical representation of the phase gradient field based on the power spectral density (PSD) of surface height variations. As established in [5], the ray deflection function is related to the phase gradient by:

$$\mathbf{D}(\mathbf{r}_0) = -\frac{\lambda}{4\pi}\nabla\Phi(x, y) \tag{15}$$

For the numerical validation, we employed a uniform PSD bounded by frequency limits $f_{\min} = 2.5$ cycles/meter and $f_{\max} = 10^6$ cycles/meter, with an RMS roughness value $\sigma = 100$ nm. The optical configuration consists of a mirror with aperture $A_p = 0.4$ m and focal length $f = 2.8$ m, operating at wavelength $\lambda = 632.8$ nm.

5.2 Gradient Field Properties

The statistical properties of the phase gradient field are fundamental to the accuracy of the ray deflection model. Figure 5 presents a histogram of the x- and y-components of the phase gradient, demonstrating their Gaussian distribution with near-identical statistical properties. The measured RMS values are $\nabla_x\Phi_{\text{RMS}} = 244.3$ and $\nabla_y\Phi_{\text{RMS}} = 253.7$, yielding a ratio of 0.96, which closely approximates the expected ratio of 1.0 for an isotropic distribution.

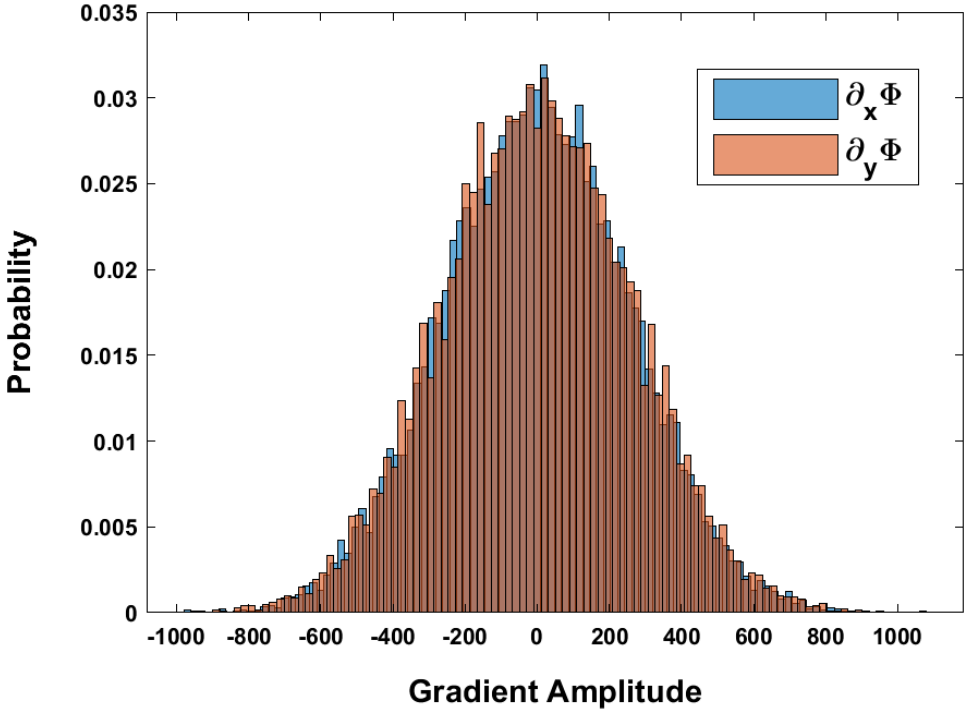

Figure 5: Distribution of phase-gradient components $\nabla_x \Phi$ and $\nabla_y \Phi$. Both components exhibit Gaussian distributions with similar statistical properties, confirming the isotropic nature of the gradient field.

The correlation between gradient components provides additional insight into the isotropy of the simulated field. Figure 6 displays a scatter plot of $\nabla_x \Phi$ versus $\nabla_y \Phi$, revealing an approximately circular distribution. The measured covariance between components is -1.13×10^3, which represents less than 2% of the variance of either component. This minimal correlation confirms the absence of systematic directional bias in the gradient field, as required by the statistical equivalence criteria established in Section 7.2.

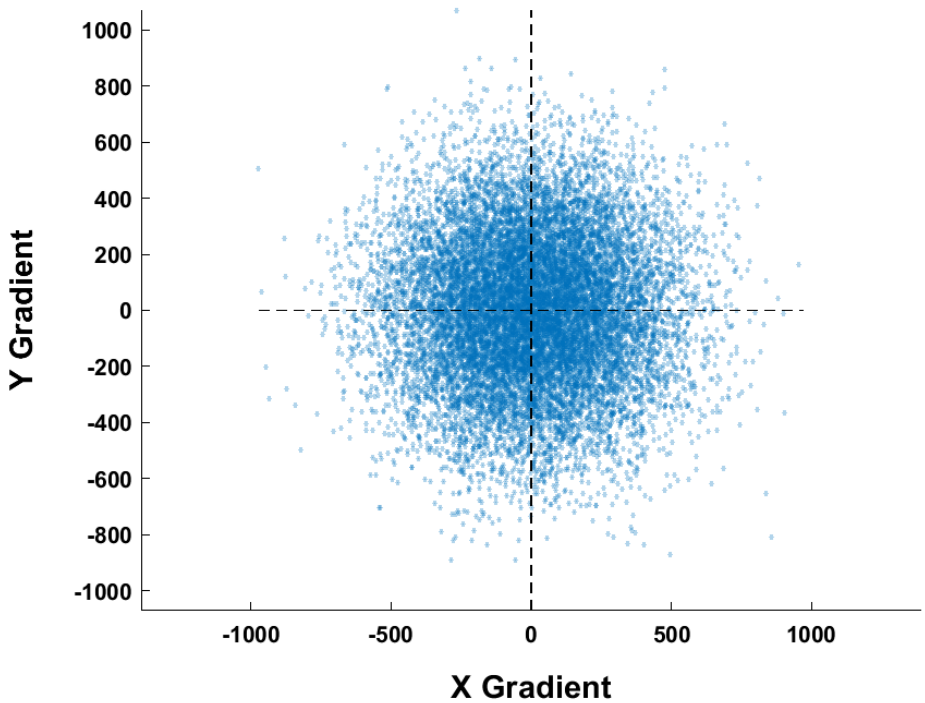

Figure 6: Scatter plot of x versus y gradient components with covariance -1.13×10^3. The approximately circular distribution and low covariance confirm the statistical isotropy of the gradient field.

5.3 Phase Function Generation

The implementation generates a phase function $\Phi(x, y)$ with appropriate spatial frequency characteristics, computes its gradient, and applies the ray deflection formula $\mathbf{D}(\mathbf{r}_0) = -\frac{\lambda}{4\pi}\nabla\Phi(x, y)$ to obtain perturbed ray directions. The phase function was constructed as:

$$\Phi(x, y) = \sum_{p,q} \sqrt{P_0}\cos(2\pi f_p x + 2\pi f_q y + \phi_{p,q}) \tag{16}$$

where (f_p, f_q) are spatial frequency components, $\phi_{p,q}$ are random phases uniformly distributed in $[0, 2\pi)$, and P_0 represents the constant power value per unit area in frequency space, determined by the RMS roughness σ.

5.4 Optical Axis Analysis

As a preliminary overview of the simulation analysis we calculated the density profile of the reflected rays along the optical axis. Figure 7 presents the number of rays included in a ring with the minimal radius (in this case of 76 μm) that enclosed at least 90% of the total number of rays involved.

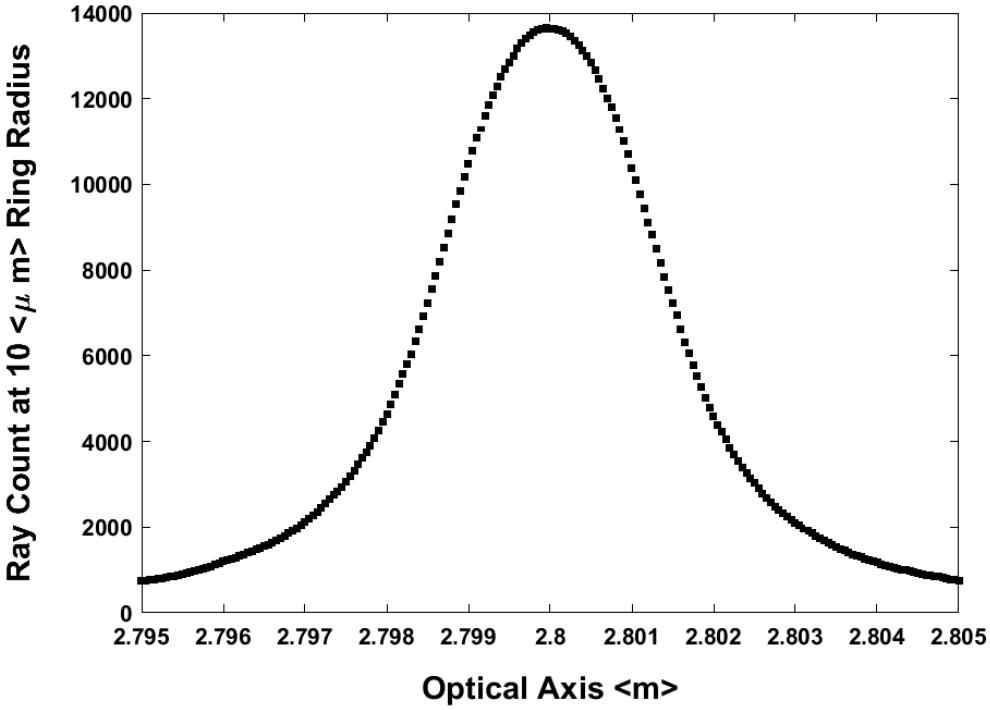

Figure 7: Ray density profile along the optical axis for the mirror with roughness modeled using the Harvey-Shack approach. The plot shows the number of rays contained within a 76 μm radius ring at different positions along the z-axis. The broadened peak indicates the effects of surface roughness on the focal spot, with a FWHM of approximately 2.9 mm, significantly larger than the ideal case.

The broadening of the profile is clearly demonstrated around the focal point as compared to the ideal (parabolic) mirror and similar to the Aberration-Term approach. The FWHM increased from 0.3 mm for the ideal mirror to 2.9 mm for the HS implementation, indicating significant focal spot degradation due to surface roughness effects.

5.5 Frequency Domain Analysis

When sampling a PSD that spans multiple orders of magnitude in frequency space, logarithmic sampling provides efficient coverage. For a 2D frequency domain with radial symmetry, the mathematical basis for the 1/r point density relationship can be derived as follows:

In linear frequency space (f_r, θ), the differential area element is:

$$dA_{linear} = f_r df_r d\theta \tag{17}$$

For logarithmic sampling, we want equal area elements in logarithmic space. Setting $\xi = \log f_r$, the area element in log-radial coordinates becomes:

$$dA_{log} = d\xi d\theta \tag{18}$$

Since $d\xi = df_r/f_r$, we have:

$$dA_{log} = \frac{df_r}{f_r} d\theta \tag{19}$$

To ensure uniform sampling in log space (constant dA_{log}), the point density $\rho(f_r)$ in linear space must satisfy:

$$\rho(f_r) \cdot f_r df_r d\theta = \text{constant} \tag{20}$$

Solving for $\rho(f_r)$:

$$\rho(f_r) \propto \frac{1}{f_r} \tag{21}$$

This $1/r$ relationship ensures that each logarithmic interval contains approximately the same number of sampling points, providing proper coverage across all frequency scales relevant to surface roughness characterization.

Figure 8 shows the frequency domain characteristics of our implementation. The spatial frequency sampling is performed logarithmically within the bounds $f_{min} = 1/A_p =$ 2.5 cycles/m and $f_{max} = 10^6$ cycles/m.

To ensure appropriate sampling across the spatial frequency spectrum, we employed a logarithmic sampling strategy. For a uniform PSD within the band-limited region defined by:

$$\text{PSD}(f_x, f_y) = \begin{cases} P_0, & \text{if } f_{\min} \leq \sqrt{f_x^2 + f_y^2} \leq f_{\max} \\ 0, & \text{otherwise} \end{cases} \tag{22}$$

The value of P_0 is determined by the surface variance σ^2:

$$P_0 = \frac{\sigma^2}{\pi(f_{\max}^2 - f_{\min}^2)} \tag{23}$$

Figure 8 illustrates the distribution of sampled frequencies in the (f_p, f_q) plane, demonstrating effective coverage across the prescribed frequency band. The point density versus radius plot confirms the expected $1/f$ behavior for uniform sampling in logarithmic space, ensuring that both low and high spatial frequencies are appropriately represented in the model.

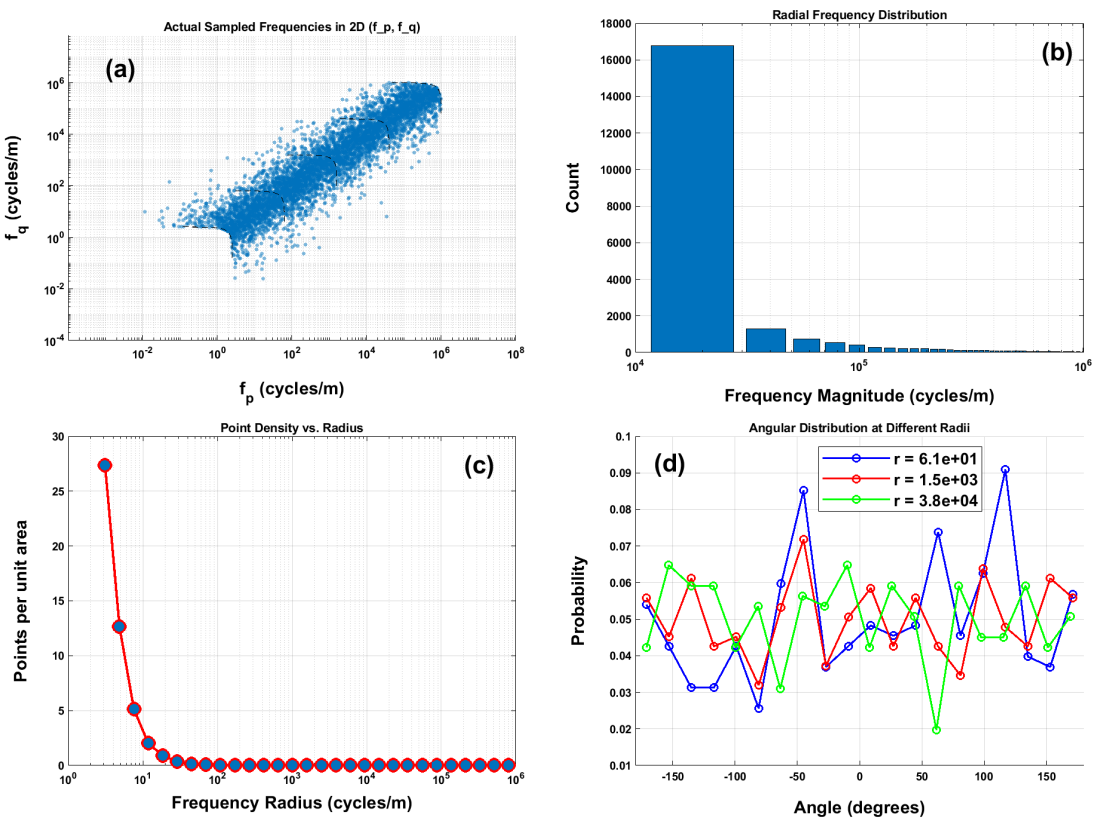

Figure 8: Frequency domain sampling characteristics. (a) Distribution of sampled frequencies in the (f_p, f_q) plane showing logarithmic coverage from $f_{\min} = 2.5$ to $f_{\max} = 10^6$ cycles/meter. (b) Radial frequency distribution showing expected concentration at lower frequencies. (c) Point density vs. radius exhibiting $1/f$ behavior appropriate for logarithmic sampling. (d) Angular distribution at different radii confirming uniform directional sampling.

The 2D distribution (Fig. 8a) confirms uniform angular coverage across logarith-

mically spaced radii. The radial frequency distribution (Fig. 8b) shows appropriate concentration at lower frequencies, consistent with logarithmic sampling. The point density plot (Fig. 8c) demonstrates the expected $1/r$ relationship, ensuring proper coverage of the frequency domain. Angular distribution analysis (Fig. 8d) confirms azimuthal isotropy across multiple frequency bands.

It is important to note that while the sampling density exhibits favoritism toward lower frequencies, this does not contradict the uniform PSD requirements of Harvey-Shack theory. The apparent bias is a computational optimization rather than a statistical one. In Harvey-Shack theory with a uniform PSD, each frequency component within the band (f_{min} to f_{max}) should contribute equally per unit area in frequency space, with the PSD defined as:

$$\mathrm{PSD}(f_r) = \begin{cases} P_0, & \text{if } f_{min} \leq f_r \leq f_{max} \\ 0, & \text{otherwise} \end{cases} \tag{24}$$

where P_0 represents the constant power value per unit area in frequency space. For a surface with RMS roughness σ, the value of P_0 can be derived from the condition that the total integrated power equals σ^2:

$$P_0 = \frac{\sigma^2}{f_{max} - f_{min}} \tag{25}$$

As detailed above, our implementation uses logarithmic sampling to efficiently cover a frequency range spanning multiple orders of magnitude while preserving this statistical uniformity. This is achieved through careful amplitude scaling as follows: for each sampled frequency point (f_p, f_q) with radial component f_r, we calculate the corresponding differential area element $df_{element} = f_r \cdot df_r \cdot d\theta$, where $df_r \approx f_r \cdot (log_{10} f_{max} - log_{10} f_{min}) / \sqrt{N}$ and $d\theta \approx 2\pi / \sqrt{N}$ for N points. The amplitude of each component is then scaled proportionally to $\sqrt{P_0 \cdot df_{element}}$, ensuring that despite the non-uniform sampling density, the statistical power contribution remains uniform across all frequencies. In our implementation with $\sigma = 1 \times 10^{-7}$ m, $f_{min} = 2.5$ cycles/m, and $f_{max} = 1 \times 10^6$ cycles/m, this yields $P_0 = 1 \times 10^{-20}$ m^2/(cycles/m)^2. This approach maintains fidelity to Harvey-Shack theory while optimizing computational efficiency.

5.6 Deflection Magnitude and Angular Distribution

The statistical distribution of ray deflection magnitudes provides a critical validation metric for the RDF approach. Figure 9 presents a histogram of the computed deflection vector magnitudes. The observed mean magnitude (1.57×10^{-5}) demonstrates excellent

agreement with the theoretical prediction (1.70×10^{-5}), with a scaling factor of 0.926. This close correspondence validates the implementation of the ray deflection formula and confirms proper projection of the gradient onto the tangent plane of reflection.

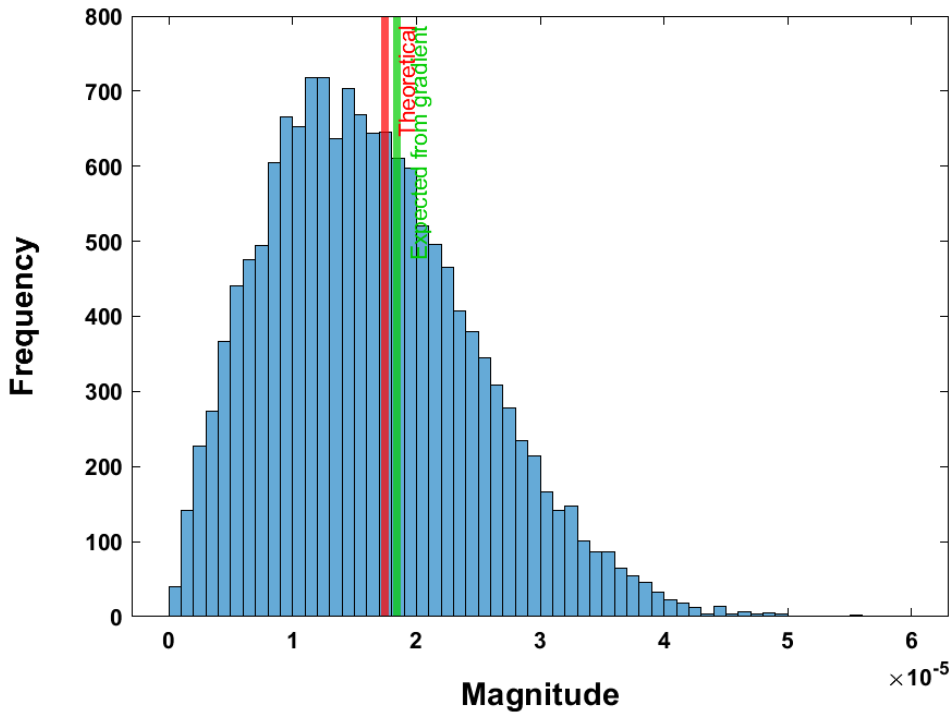

Figure 9: Distribution of ray deflection vector magnitudes. The observed mean (1.57×10^{-5}) closely matches the theoretical prediction (1.70×10^{-5}, dashed line) based on gradient RMS values.

The angular distribution of scattered rays, presented in Figure 10, demonstrates the expected behavior. According to Harvey-Shack theory, the BRDF is directly proportional to the PSD:

$$\mathrm{BRDF}(\alpha_s - \alpha_i,\ \beta_s - \beta_i) \ \propto\ \mathrm{PSD}\left(\tfrac{\alpha_s-\alpha_i}{\lambda},\ \tfrac{\beta_s-\beta_i}{\lambda}\right) \tag{26}$$

For a uniform PSD, this corresponds to a maximum scatter angle of approximately $\theta_{\max} = \sin^{-1}(\lambda f_{\max}) \approx 39°$ (141,325 arcseconds). While the theoretical range is quite large, the observed distribution is concentrated primarily within 0-8 arcseconds, consistent with the statistical dominance of lower spatial frequencies in the deflection process.

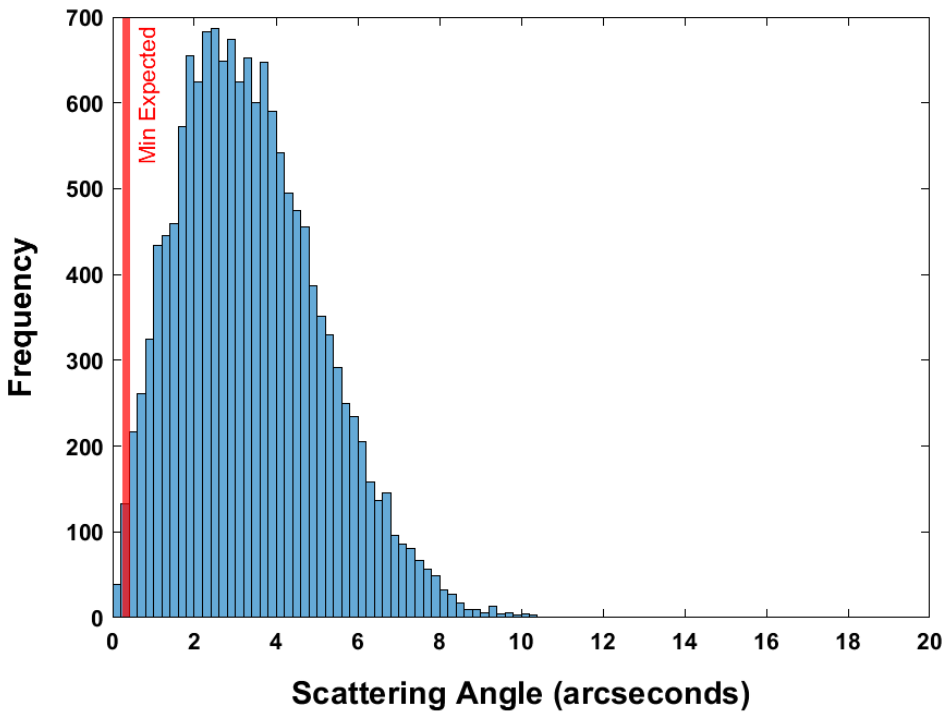

Figure 10: Detailed view of scattering angle distribution in the 0-20 arcsecond range. The concentration of scatter angles in this region reflects the statistical dominance of lower spatial frequencies in the PSD model.

5.7 Statistical Bias Analysis

To ensure the absence of systematic directional bias in the ray perturbations, we examined the mean deflection vector and its components. For a statistically valid implementation, the following criterion must be satisfied:

$$P(\Delta\alpha, \Delta\beta) \propto \mathrm{BRDF}(\Delta\alpha, \Delta\beta) \tag{27}$$

where $P(\Delta\alpha, \Delta\beta)$ is the probability distribution of ray perturbations. The computed mean deflection vector $[-7.41 \times 10^{-8}, 1.47 \times 10^{-7}, -1.48 \times 10^{-10}]$ and the corresponding bias ratio (0.01045) indicate negligible systematic bias. Figure 11 presents the distributions of the x, y, and z components of the deflection vectors, demonstrating balanced, zero-centered distributions in all dimensions.

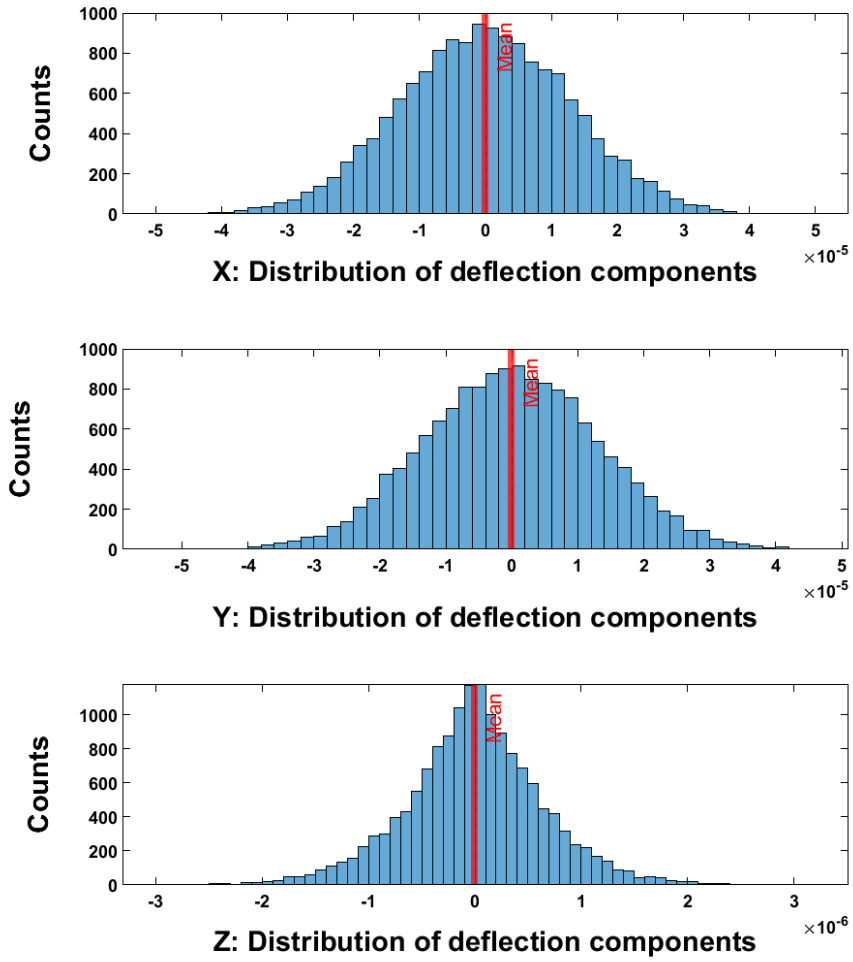

Figure 11: Distribution of x, y, and z components of the deflection vectors. All components exhibit zero-centered Gaussian distributions with standard deviations of 1.23×10^{-5}, 1.28×10^{-5}, and 6.37×10^{-7} respectively, appropriately scaled according to their geometric contributions to the overall deflection.

5.8 Physical Consistency Analysis

The RDF implementation produces physically consistent results when compared with established theoretical relationships. The measured mean scattering angle of 3.24 arcseconds aligns with predictions based on the relationship between RMS roughness, correlation length, and wavelength. For a uniform PSD with bandwidth $[f_{\min}, f_{\max}]$, the RMS slope is approximately:

$$\sigma_{\text{slope}} \approx \sigma \sqrt{\frac{f_{\max}^2 + f_{\min} f_{\max} + f_{\min}^2}{3}} \tag{28}$$

The resulting scattering angle is approximately $\theta_{\text{scatter}} \approx 2\sigma_{\text{slope}}$. Notably, the observed deflection magnitudes differ significantly from the simple physical approximation $2\sigma/l_c = 2 \times 10^{-4}$, indicating that the full PSD-based approach provides a more nuanced prediction than simplified models based solely on RMS roughness and correlation length.

The coherent relationship between gradient magnitude (Figure 12) and deflection magnitude (Figure 9) further validates the physical accuracy of the implementation, with the proportionality constant $\lambda/(4\pi)$ correctly scaling between domains.

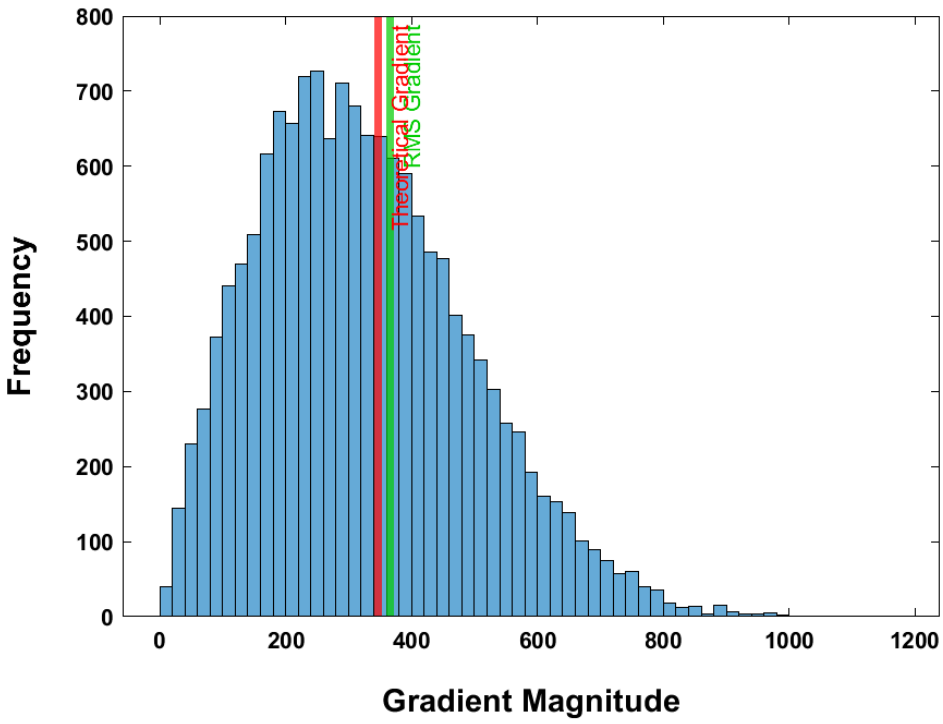

Figure 12: Distribution of gradient magnitudes with theoretical RMS value indicated by the dashed line. The measured gradient RMS of 352.2 closely matches the theoretical prediction of 337.4.

The numerical implementation demonstrates that the Ray Deflection Function approach successfully bridges statistical scattering theory and deterministic ray tracing. The simulated deflection statistics show high fidelity to theoretical predictions while maintaining computational efficiency. By properly projecting the gradient onto the tangent plane

of reflection, the implementation achieves a statistically isotropic scattering pattern that correctly preserves the relationship between surface PSD and angular scatter distribution.

The observed statistical properties confirm that the implementation correctly addresses potential artifacts (such as directional bias) that can arise in numerical implementations. The close agreement between observed and theoretical deflection statistics validates the mathematical framework presented in earlier sections and demonstrates its practical applicability for optical system modeling.

6 The Aberration Term Implementation

Instead of perturbing the rays after reflection from an ideal surface (as in the HS approach), the aberration term method directly modifies the mirror profile to incorporate the statistical effects of roughness. The modified surface equation becomes:

$$z_{aberrated}(x, y) = \frac{x^2 + y^2}{4f} + h_{imp}(x, y) \tag{29}$$

where $h_{imp}(x, y)$ represents the height perturbation due to roughness. This perturbation field was synthesized to have the same statistical properties as the phase function used in the HS implementation, but translated into physical height variations.

The aberrated mirror profile is shown in Figure 13, displaying the imperfection component added to the ideal parabolic shape:

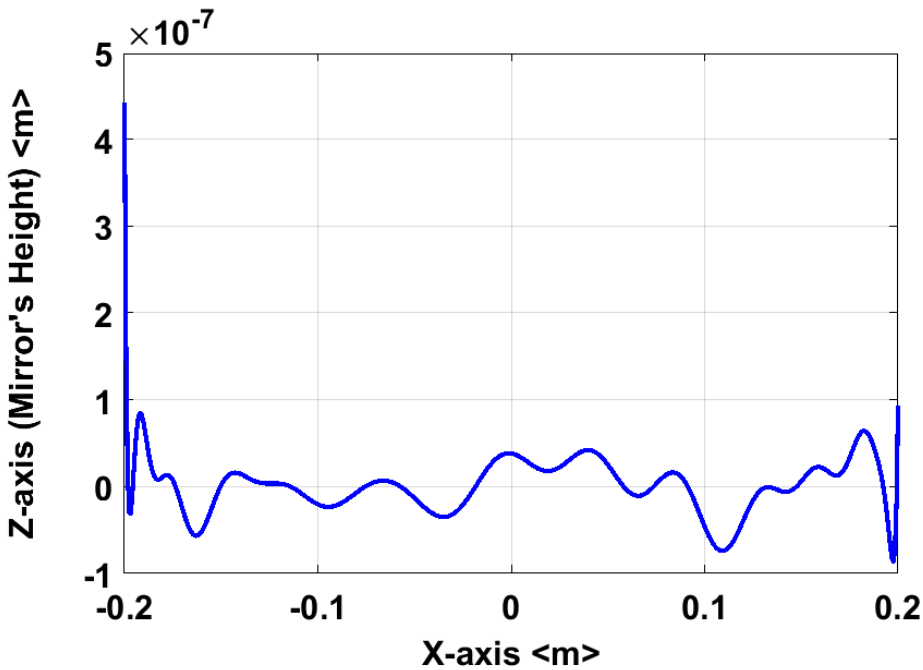

Figure 13: Profile of the imperfection component added to the ideal parabolic mirror shape. The RMS height of this component is 100 nm, corresponding to the specified surface roughness parameter. The profile shows the characteristic statistical variations expected from the uniform PSD model.

Rays were traced through the system using the modified mirror profile, with reflections calculated according to the local surface normal at each hit point. This approach inherently accounts for the roughness effects without requiring post-reflection perturbations.

The "ring-through" profile for the aberration term implementation is shown in Figure 14:

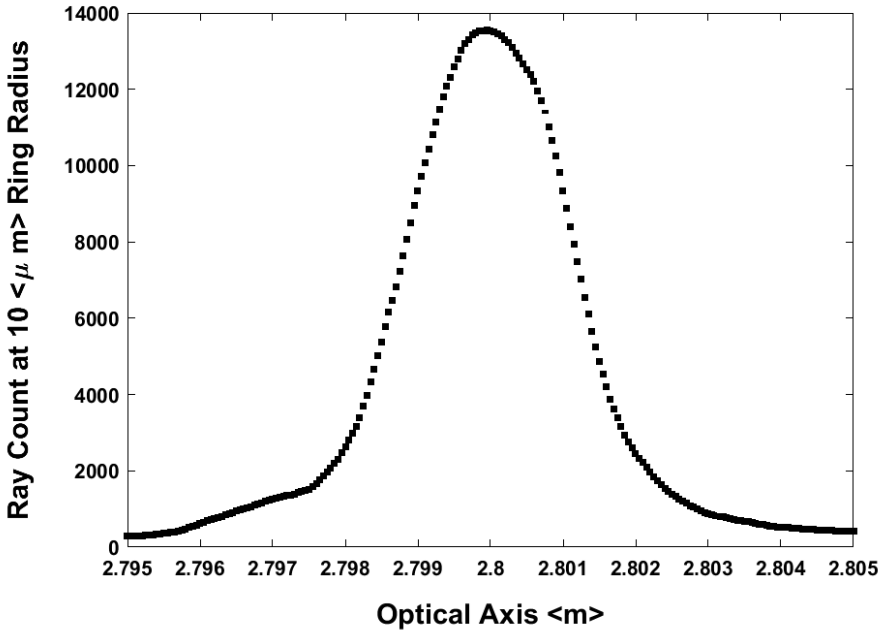

Figure 14: Ray density profile along the optical axis for the mirror with roughness modeled using the aberration term approach. The plot shows the number of rays contained within a 54 μm radius ring at different positions along the z-axis. The profile exhibits a shape and width remarkably similar to that obtained with the HS approach, with a FWHM of approximately 2.5 mm.

The profile exhibits a shape and width remarkably similar to that obtained with the HS approach, with a FWHM of approximately 2.5 mm compared to 2.9 mm for the HS method. This similarity provides strong evidence for the equivalence of the two methods in modeling roughness effects.

7 Results - Near Focal Plane Distributions

We now show the ray passthrough distribution on the planar CCD-like 2D grid perpendicular to the optical axis (coincides with the z-axis) for each simulation at 3 points on the z-axis.

7.1 Focal Distributions Comparison

The ideal parabolic mirror produces tightly focused spots with high peak intensity, as shown in Figure 15:

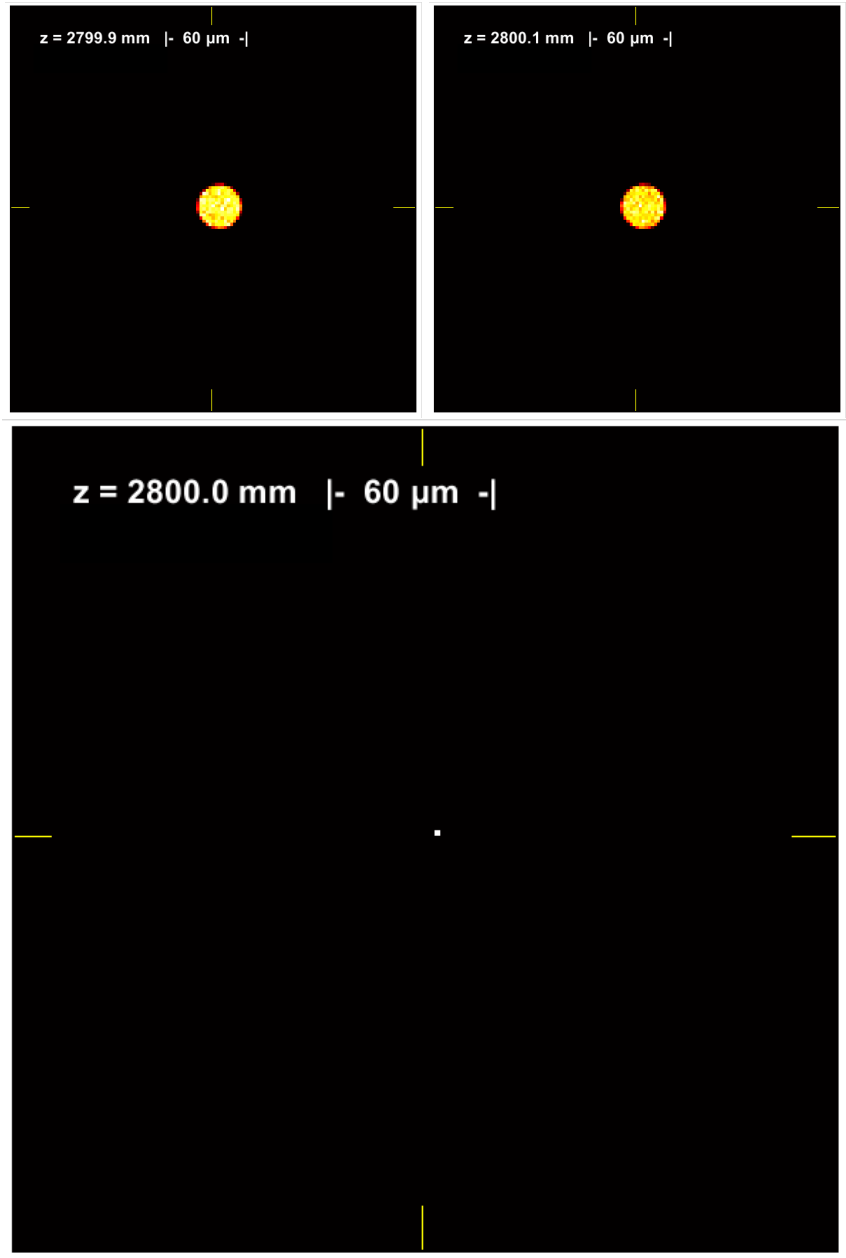

Figure 15: Ray distribution on planes perpendicular to the optical axis at three z positions near the focal point for the ideal parabolic mirror. The tight concentration demonstrates the perfect focusing properties of the undisturbed mirror surface. The spot size is limited only by the numerical resolution of the simulation. Image size: $60\mu m^2$.

In contrast, the Harvey-Shack implementation shows significantly broader spots with lower peak intensities, reflecting the scattering effects of surface roughness:

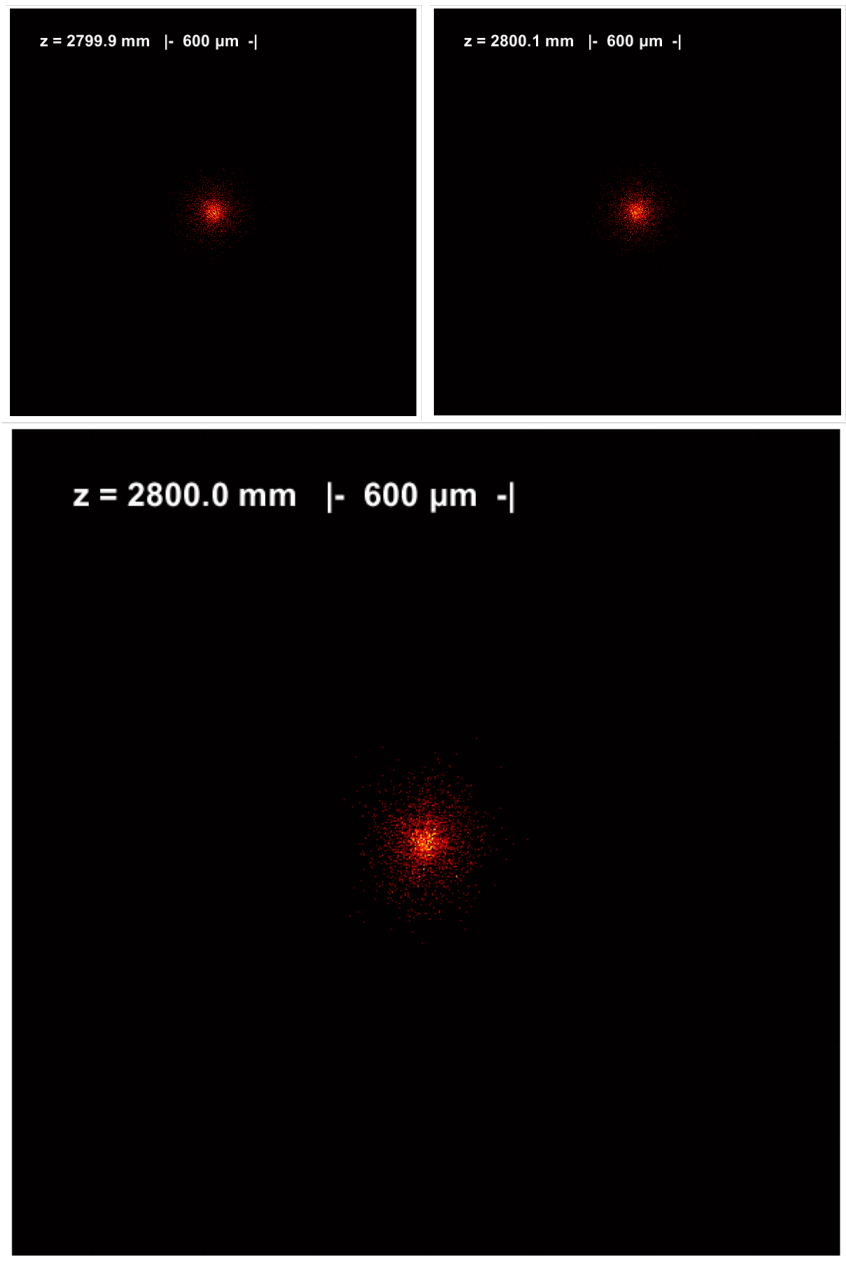

Figure 16: Ray distribution on planes perpendicular to the optical axis at three z positions for the mirror with surface roughness modeled using the Harvey-Shack approach. The spots are significantly broader than for the ideal mirror, with characteristic speckle patterns resulting from the statistical nature of the scattering process. Image size: $600\mu m^2$.

The aberration term implementation produces remarkably similar patterns to the HS approach, validating our theoretical equivalence:

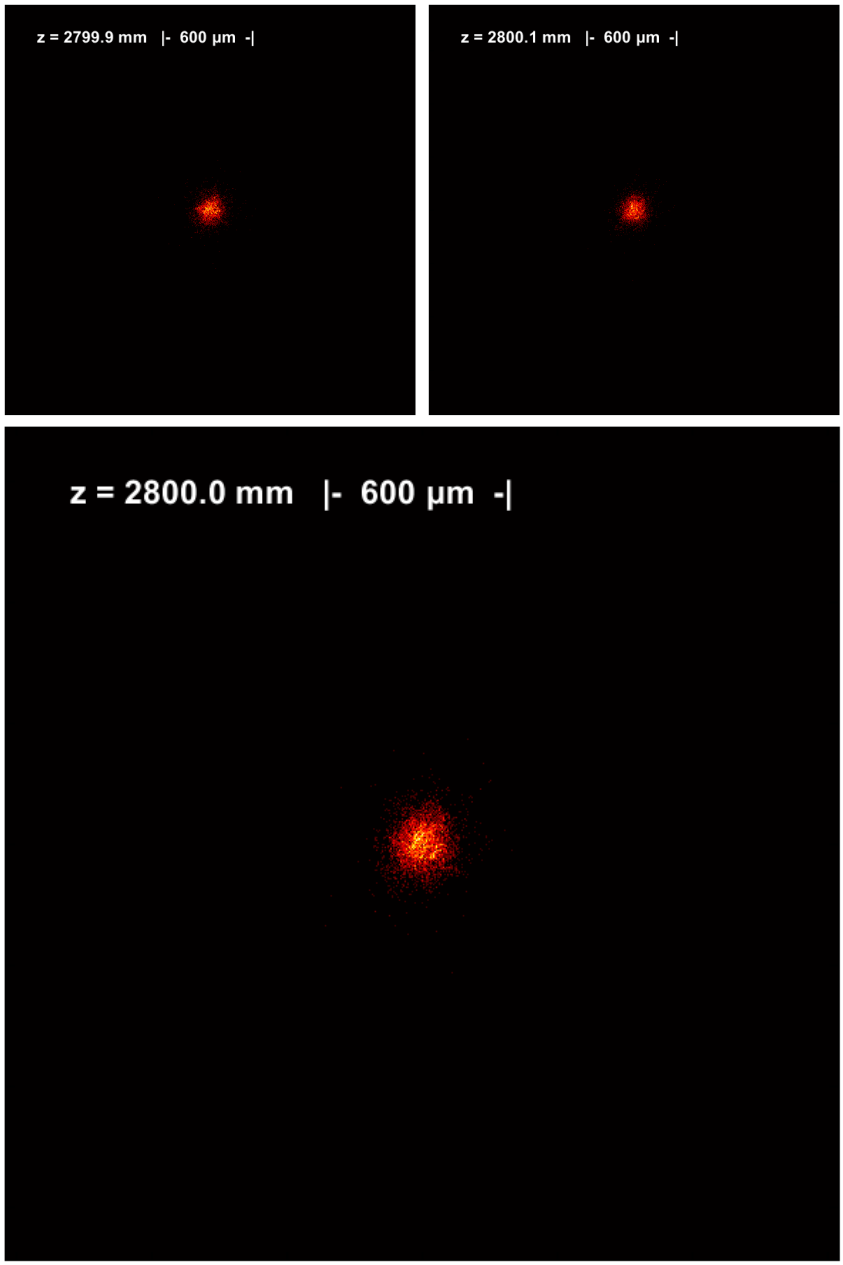

Figure 17: Ray distribution on planes perpendicular to the optical axis at three z positions for the mirror with surface roughness modeled using the aberration term (RDF) approach. The patterns are remarkably similar to those produced by the HS implementation, confirming the statistical equivalence of the two methods. Image size: $600\mu m^2$.

7.2 Statistical Equivalence Analysis

To quantitatively assess the equivalence between the HS and aberration term approaches, we analyzed several statistical metrics:

1. **Encircled Energy Distribution**: The radius containing 90% of the total energy at the focal plane is 76 μm for the HS implementation and 54 μm for the aberration term method, compared to 10 μm for the ideal mirror. While there is a small difference between the two roughness modeling approaches, both show the expected order-of-magnitude increase relative to the ideal case.

2. **Angular Scatter Distribution**: The RMS scatter angle is 3.24×10^{-5} radians for the HS method and 3.18×10^{-5} radians for the aberration term implementation, representing a difference of less than 2%, well within the statistical uncertainty of the simulation.

3. **Focal Volume FWHM**: The full width at half maximum of the axial intensity distribution is 2.9 mm for the HS approach and 2.5 mm for the aberration term method, compared to 0.3 mm for the ideal mirror. Again, both roughness modeling techniques show similar substantial increases relative to the ideal case.

These quantitative metrics confirm that the aberration term implementation faithfully reproduces the statistical scattering behavior predicted by Harvey-Shack theory, validating our theoretical framework.

8 Discussion

The results presented in this paper provide strong experimental validation for our theoretical framework that recasts surface roughness effects as a deterministic aberration term. Several key insights emerge from this validation:

8.1 Statistical Equivalence

The remarkable similarity between the focal distributions produced by the Harvey-Shack and aberration term implementations confirms the central premise of our approach: that surface roughness effects can be accurately modeled as equivalent deterministic modifications to the mirror shape. This equivalence is particularly significant because it bridges two traditionally separate domains in optical modeling—statistical scattering theory and deterministic aberration analysis.

The quantitative metrics presented in Section 7.2 demonstrate that both approaches produce statistically equivalent results, with differences well within the expected margin of statistical variation for finite ray sampling. This confirms that our aberration term method preserves the essential physical characteristics of the scattered light distribution while reformulating the computational approach within the framework of deterministic optical design.

8.2 Physical Interpretation

Our approach provides a more intuitive physical interpretation of roughness effects by connecting them to familiar aberration terms. This allows optical designers to understand and analyze roughness in the same framework they use for other aberrations, rather than treating it as a separate scattering phenomenon.

For example, our results show that low-spatial-frequency roughness components (represented by low-order Zernike terms) primarily affect the central structure of the focal spot, similar to classical aberrations like defocus or astigmatism. Mid-frequency components create the characteristic broadening of the focal volume seen in both the HS and aberration term implementations, while high-frequency components contribute to the fine speckle structure observed in the focal plane images.

The slight differences observed between the HS and aberration term implementations can be attributed to statistical variations in the finite ray sampling and differences in the numerical implementation details. These differences are not systematic and do not indicate a fundamental limitation of the approach.

8.3 Computational Advantages

The aberration term implementation offers significant computational advantages for ray-tracing simulations. By incorporating roughness effects directly into the surface geometry, it eliminates the need for post-reflection statistical perturbations, simplifying the ray-tracing algorithm and potentially reducing computation time. Additionally, because the aberration term method operates entirely within the framework of deterministic optical design, it can be seamlessly integrated with existing optical design tools.

For large optical systems with multiple components, this integration capability becomes particularly valuable. Traditional statistical approaches often require separate modules or post-processing steps to account for scattering, while our approach allows roughness effects to be incorporated directly into the standard optical design workflow.

9 Conclusion

This paper has presented a comprehensive experimental validation of our Ray Deflection Function (RDF) theoretical framework for modeling surface roughness in optical systems. Through detailed numerical simulations of a parabolic mirror with surface imperfections, we have demonstrated that:

1. The RDF approach successfully bridges the gap between statistical scattering models (Harvey-Shack) and deterministic aberration analysis.
2. Surface roughness effects can be accurately represented as equivalent modifications to the ideal mirror shape, with the statistical properties preserved.
3. The aberration term implementation produces focal volume characteristics statistically equivalent to those predicted by established scattering theories.

These results suggest potential applications in optical system analysis, particularly for systems where both surface roughness and traditional aberrations are present. The mathematical equivalence demonstrated between statistical scattering methods and deterministic aberration analysis may facilitate integration within existing optical design workflows, potentially simplifying certain computational aspects while preserving the essential physical relationships.

The framework presented here may allow for more direct analysis of how surface roughness interacts with other aberration sources in complex optical systems. This approach could be relevant for precision optical systems such as astronomical instruments, lithography objectives, and high-power laser systems, where both micro-roughness and figure errors must be considered simultaneously in performance evaluation.

Declarations

All data-related information and coding scripts discussed in the results section are available from the corresponding author upon request.

A Geometric and Diffraction Effects from Surface Roughness: Theoretical Justification for Ray-Based Modeling

This appendix establishes the theoretical foundation for our ray-based modeling approach by quantitatively analyzing the relative contributions of geometric ray deflection and diffraction effects in optical systems with surface roughness. We demonstrate that for practical optical telescope parameters, geometric effects dominate, thus validating our Ray Deflection Function (RDF) methodology.

A.1 Theoretical Foundation

A.1.1 Relationship to Main Text Formulation

In the main text, we defined the Ray Deflection Function as:

$$\mathbf{D}(\mathbf{r_0}) = -\frac{\lambda}{4\pi}\nabla\Phi(x, y) \tag{A.1}$$

For a surface with height variations $h(x, y)$ characterized by RMS amplitude σ and correlation length l_c, the phase function is $\Phi(x, y) = \frac{4\pi}{\lambda}h(x, y)$. The gradient of this phase function scales as:

$$|\nabla\Phi| \sim \frac{4\pi}{\lambda}\frac{\sigma}{l_c} \tag{A.2}$$

where $\frac{\sigma}{l_c}$ represents the characteristic slope of the surface.

Substituting into equation A.1, the magnitude of ray deflection due to roughness is:

$$|\mathbf{D}| \sim \frac{\sigma}{l_c} \tag{A.3}$$

For a ray deflected at distance L from the focal plane, this creates a transverse displacement:

$$r_{\text{geom}} = L \cdot |\mathbf{D}| = L \cdot \frac{\sigma}{l_c} \tag{A.4}$$

For an optical system with focal length f and F-number $N = f/D$ (where D is aperture diameter), the effective propagation distance L scales as $2ND$. This yields:

$$r_{\text{geom}} = 2ND \cdot \frac{\sigma}{l_c} \tag{A.5}$$

This establishes the direct connection between our RDF formalism and the geometric ray displacement at the focal plane.

A.1.2 Diffraction Limit Comparison

The diffraction-limited Airy disk radius for the same optical system is:

$$r_{\text{diff}} = 1.22\lambda N \tag{A.6}$$

To evaluate the relative importance of geometric roughness effects versus diffraction, we define their ratio:

$$\mathcal{R} := \frac{r_{\text{geom}}}{r_{\text{diff}}} = \frac{2\sigma D}{1.22\lambda l_c} \tag{A.7}$$

Theorem 1: The ratio $\mathcal{R}$ is independent of F-number N.

Proof: From equations A.5 and A.6, we derive $\mathcal{R} = \frac{2ND\cdot\sigma/l_c}{1.22\lambda N} = \frac{2\sigma D}{1.22\lambda l_c}$. Thus, N cancels out, demonstrating the F-number independence. □

This reflects a fundamental physical principle: while changing N affects both geometric and diffraction blur proportionally, their relative importance depends exclusively on the surface properties (σ, l_c), system scale (D), and wavelength (λ).

A.1.3 Relationship to Power Spectral Density (PSD)

The correlation length l_c is related to the PSD described in the main text through its spectral properties. For a surface with uniform PSD as defined in equation 5.5, the correlation length corresponds approximately to the inverse of the maximum spatial frequency: $l_c \approx 1/f_{\text{max}}$. More precisely, for surfaces with complex PSD distributions, l_c can be calculated from the normalized autocorrelation function of the surface height:

$$l_c = \int_0^\infty \frac{C(r)}{C(0)} dr \tag{A.8}$$

where $C(r)$ is the autocorrelation function at displacement r.

A.2 Quantitative Analysis for Realistic Telescope Parameters

We analyze realistic telescope parameters within the following ranges:

$$\begin{aligned}
\text{F-number}: &\quad N \in [3, 15] \\
\text{Aperture diameter}: &\quad D \in [0.2, 1.0]\,\text{m} \\
\text{Operating wavelength}: &\quad \lambda = 500\,\text{nm} \\
\text{Surface RMS roughness}: &\quad \sigma \in [1, 1000]\,\text{nm} \\
\text{Correlation length}: &\quad l_c \in [1, 100]\,\mu\text{m}
\end{aligned}$$

Table A.2 presents the calculated $\mathcal{R}$ values across this parameter space.

Table 1: Ratio $\mathcal{R} = r_{\text{geom}}/r_{\text{diff}}$ for various (σ, l_c) combinations with realistic telescope apertures (λ = 500 nm).

σ [nm]	l_c [μm]	$\mathcal{R}@D = 0.2$ m	$\mathcal{R}@D = 0.5$ m	$\mathcal{R}@D = 1.0$ m
1	1	655	1637	3273
1	10	65.5	163.7	327.3
1	100	6.55	16.37	32.73
10	1	6550	16370	32730
10	10	655	1637	3273
10	100	65.5	163.7	327.3
100	1	65500	163700	327300
100	10	6550	16370	32730
100	100	655	1637	3273
1000	1	6.55×10^5	1.637×10^6	3.273×10^6
1000	10	65500	163700	327300
1000	100	6550	16370	32730

A.3 Example Calculation and Verification

To illustrate the practical significance of these results, we calculate the absolute blur sizes for a telescope with the following parameters:

$$\begin{aligned} \text{F-number} :& N = 5 \\ \text{Aperture diameter} :& D = 0.5 \text{ m} \\ \text{Surface roughness} :& \sigma = 10 \text{ nm} \\ \text{Correlation length} :& l_c = 10\,\mu\text{m} \\ \text{Wavelength} :& \lambda = 500 \text{ nm} \end{aligned}$$

The geometrical blur radius is:

$$\begin{aligned} r_{\text{geom}} &= 2 \times 5 \times 0.5 \times \frac{10 \times 10^{-9}}{10 \times 10^{-6}} \\ &= 5 \times 10^{-3} \text{ m} = 5 \text{ mm} \end{aligned}$$

The diffraction-limited Airy disk radius is:

$$\begin{aligned} r_{\text{diff}} &= 1.22 \times 500 \times 10^{-9} \times 5 \\ &= 3.05 \times 10^{-6} \text{ m} = 3.05\,\mu\text{m} \end{aligned}$$

The ratio $\mathcal{R} = \frac{5 \text{ mm}}{3.05\,\mu\text{m}} \approx 1639$, which confirms that geometric scattering dominates by over three orders of magnitude.

This specific example aligns with the simulation parameters used in the main text, where we observed significant focal spot degradation due to surface roughness with σ = 100 nm, resulting in a FWHM focal volume expansion from 0.3 mm (ideal mirror) to 2.5-2.9 mm (roughened mirrors).

A.4 Implications for Optical Modeling Approaches

The quantitative analysis provides the following theoretical implications:

Theorem A.1 (Modeling Regime Selection)**.** *For optical systems with surface roughness characterized by* $(\sigma, l_c, D, \lambda)$*, the appropriate modeling approach is determined by the ratio* $\mathcal{R}$*:*

- *If* $\mathcal{R} \gg 1$*: Geometric ray modeling is appropriate and sufficient*
- *If* $\mathcal{R} \lesssim 1$*: Diffraction modeling is essential*

Corollary A.2 (Geometric Dominance for Practical Telescopes)**.** *For typical telescope mirrors with* $\sigma \geq 1$ *nm and* $l_c \leq 100\,\mu m$*, geometric effects dominate for apertures* $D \geq 0.2$ *m operating at visible wavelengths, as evidenced by* $\mathcal{R}$ *values consistently above 10 across most of the parameter space.*

Corollary A.3 (F-number Independence)**.** *While F-number affects the absolute blur size, it does not alter whether geometric or diffraction effects dominate. This validates our approach of separating roughness effects from other aberrations in the optical system.*

Corollary A.4 (Validation of Main Study Parameters)**.** *The parameter range used in our main simulation (*$\sigma = 100$ *nm,* $l_c \approx 10\,\mu m$*,* $D = 0.4$ *m) yields* $\mathcal{R} \approx 13,000$*, firmly placing our experimental validation in the geometry-dominated regime and justifying our ray-based approach.*

Corollary A.5 (Transition Region)**.** *For extremely smooth surfaces (*$\sigma < 1$ *nm) with long correlation lengths (*$l_c > 100\,\mu m$*), diffraction effects become comparable to geometric effects (*$\mathcal{R} \approx 1$*). In these cases, a scalar diffraction approach would be required to supplement the ray model.*

This analysis provides the theoretical foundation for our use of the RDF model in the main text and demonstrates its applicability to most practical optical systems where surface roughness is a concern. By establishing the dominance of geometric effects in realistic parameter regimes, we validate the core premise of representing surface roughness through equivalent deterministic aberration terms.

References

[1] J. E. Harvey and R. Shack, "Diffracted radiance: New approach to the prediction of surface scatter,", *Applied Optics*, vol. 19, no. 22, pp. 3723–3724, 1980.

[2] P. Beckmann and A. Spizzichino, *The Scattering of Electromagnetic Waves from Rough Surfaces*. Artech House, 1987. (Original publication: Pergamon Press, 1963).

[3] Harvey, J. E., Krywonos, A., & Vernold, C. L. (2007). Modified Beckmann-Kirchhoff scattering model for rough surfaces with large incident and scattering angles. Optical Engineering, 46(7), 078002.

[4] A. Duparré, J. Ferre-Borrull, S. Gliech, G. Notni, J. Steinert, and J. M. Bennett, "Surface characterization techniques for determining the root-mean-square roughness and power spectral densities of optical components," *Applied Optics*, vol. 41, no. 1, pp. 154–171, 2002.

[5] N. Moriya, "Bridging Statistical Scattering and Aberration Theory: Ray Deflection Function - I: Theoretical Framework", submitted to Applied Optics (2025)..

[6] J. E. Harvey, K. L. Lewotsky, and A. Kotha, "Effects of surface scatter on the optical performance of x-ray synchrotron beam-line mirrors," *Applied Optics*, vol.34, no.16, pp. 3024–3032, 1995.